

Remote Sensing Image Fusion via Sparse Representations Over Learned Dictionaries

Shutao Li, *Member, IEEE*, Haitao Yin, and Leyuan Fang, *Student Member, IEEE*

Abstract—Remote sensing image fusion can integrate the spatial detail of panchromatic (PAN) image and the spectral information of a low-resolution multispectral (MS) image to produce a fused MS image with high spatial resolution. In this paper, a remote sensing image fusion method is proposed with sparse representations over learned dictionaries. The dictionaries for PAN image and low-resolution MS image are learned from the source images adaptively. Furthermore, a novel strategy is designed to construct the dictionary for unknown high-resolution MS images without training set, which can make our proposed method more practical. The sparse coefficients of the PAN image and low-resolution MS image are sought by the orthogonal matching pursuit algorithm. Then, the fused high-resolution MS image is calculated by combining the obtained sparse coefficients and the dictionary for the high-resolution MS image. By comparing with six well-known methods in terms of several universal quality evaluation indexes with or without references, the simulated and real experimental results on QuickBird and IKONOS images demonstrate the superiority of our method.

Index Terms—Dictionary learning, image fusion, multispectral (MS) image, panchromatic (PAN) image, remote sensing, sparse representation.

I. INTRODUCTION

IN optical remote sensing, the sensors are designed following a tradeoff among spectral resolution, spatial resolution, and signal to noise. In addition, the spatial resolution of remote sensing image is always limited due to the onboard storage and bandwidth. As a result, remote sensing satellites often provide panchromatic (PAN) image with high spatial resolution and multispectral (MS) image with high spectral resolution. For example, the IKONOS satellite produces PAN image with 1-m spatial resolution and MS image with 4-m spatial resolution. Generally, remote sensing images with high spectral and high spatial resolutions are essential for complete and accurate description of the observed scene. Remote sensing image fusion is an effective technique to integrate spatial and spectral information of the PAN and MS images [1]. Through remote sensing image fusion technique, we cannot only overcome the

limitation of information obtained from individual sensor but also achieve a better observation [2].

Recently, various approaches have been proposed to address the problem of remote sensing image fusion. The existing methods can be categorized into three classes: component-substitution-based methods, multiresolution-analysis-based methods, and restoration-based methods. The representative component-substitution-based methods are the intensity–hue–saturation (IHS) [3], [4] and the principal component analysis [5]. The main steps of classical IHS-based method are as follows. First, the spectral bands of MS image are transformed into the IHS image space. Then, the intensity component is replaced by the PAN image. The final fused result is obtained by the inverse transform. The fused image obtained through the component-substitution-based methods can achieve high spatial resolution; however, spectral distortion is hard to avoid.

Multiresolution analysis provides another effective technique to fuse the PAN image and the MS image. The wavelet transform (WT)-based methods are the representative methods [6], [7]. The PAN and each band of the MS image are decomposed into high- and low-frequency components through WT. The high-frequency component extracted from the PAN image is merged into the MS bands. The fused image is obtained by performing the inverse WT. In [8], the additive wavelet luminance (AWL) method is proposed by combining the “à trous” WT (ATWT) and IHS transform. In AWL, the details from the PAN image are injected into the luminance band of the MS image. A generalized proportional AWL method termed as AWL proportional (AWLP) injects the details with self-adapting proportion [9]. Recently, other popular multiresolution-analysis-based methods have been proposed, such as the ATWT with context-based decision (CBD) injection model [10], support value transform (SVT) [11], and Laplacian pyramids [12]. Compared with the component-substitution-based methods, the multiresolution-analysis-based methods preserve better spectral information. However, the spatial distortions may occur accompanied by the blurring and artifacts [13].

With the characteristic of satellite imaging, the PAN image and MS image can be modeled as the degraded images of high-resolution MS image. Based on these imaging models, the restoration-based methods address the remote sensing image fusion problem through some optimization problems. Furthermore, the regularization terms of optimization problem are necessary for restricting the solution, such as the inhomogeneous Gaussian Markov random field prior [14] and the constrained least square [15]. In [16], Li and Yang proposed a remote sensing image fusion method based on compressive sensing (CS). With the sparsity prior information, the high-resolution

Manuscript received April 10, 2011; revised July 7, 2012, September 28, 2012, and November 13, 2012; accepted November 20, 2012. Date of publication February 1, 2013; date of current version August 30, 2013. This paper was supported in part by the National Natural Science Foundation of China under Grant 61172161, by the Fundamental Research Funds for the Central Universities, Hunan University, and by the Scholarship Award for Excellent Doctoral Student granted by the Chinese Ministry of Education.

The authors are with the College of Electrical and Information Engineering, Hunan University, Changsha 410082, China (e-mail: shutao_li@yahoo.com.cn; haitao_yin@yahoo.cn; fangleyuan@gmail.com).

Color versions of one or more of the figures in this paper are available online at <http://ieeexplore.ieee.org>.

Digital Object Identifier 10.1109/TGRS.2012.2230332

MS image is reconstructed through the CS theory. To enforce the sparsity, the dictionary used in [16] consists of image patches randomly sampled from the high-resolution MS images. If the sampled patches are enough, the constructed dictionary through this strategy contains the abundant information of remote sensing images. Nevertheless, a large dictionary often leads to expensive computation.

In this paper, we focus on the restoration approach and propose a novel method based on sparse representation over learned dictionaries. The dictionaries for PAN image and low-resolution MS image are learned from source images adaptively. Furthermore, a novel strategy is designed to construct the dictionary for high-resolution MS image from the dictionaries for PAN image and low-resolution MS image. Through our dictionary learning method, the learned dictionaries can enforce that the PAN, low-resolution MS, and high-resolution MS images have the same sparse coefficients. These sparse coefficients are sought by the orthogonal matching pursuit (OMP) algorithm. Then, the fused MS image is reconstructed by the obtained sparse coefficients and the dictionary of the high-resolution MS image. Compared with the method presented in [16], our method has the following novelties. First, instead of randomly sampled patches, we adopt the learned dictionaries, which can reduce the dimensionality of dictionary, speed up the sparse decomposition, and improve the effectiveness and robustness of remote sensing image fusion. Second, we learn that the dictionaries are learned from the source images directly, which can improve the adaptability of dictionaries. Third, in our method, the dictionary for high-resolution MS image is constructed from the dictionaries for PAN image and low-resolution MS image, which does not need the high-resolution MS training set. This strategy makes our method more practical. Generally, the choice of dictionary is crucial for sparse representation, which affects the performance of sparse representation directly. Therefore, the aforementioned three novelties indicate that our method has significant improvements over [16].

This paper is organized as follows. In Section II, we briefly review the theory of sparse representation. The proposed method is presented in Section III. In particular, the relationships of the PAN image and low-resolution MS image from the unknown high-resolution MS image are modeled. Then, the corresponding dictionary learning and construction strategy are discussed. The experimental results and comparisons are given in Section IV. The conclusions are drawn in Section V.

II. SPARSE REPRESENTATION

Sparse representation is a powerful tool to describe signals, which derives from the mechanism of human vision [17]. Recently, sparse representation has attracted much interest and has been applied into many image processing areas, such as image denoising [18] and image superresolution [19].

Generally, nature image contains complicated and nonstationary information as a whole, while local small image patch appears simple and has a consistent structure. For this reason, the small patch can be modeled more easily than the whole image. Let $\mathbf{x} \in \mathbb{R}^n$ be a $\sqrt{n} \times \sqrt{n}$ image patch ordered lexi-

cographically as column vector. In sparse representation theory, the patch \mathbf{x} can be represented as a sparse linear combination of the columns with respect to a dictionary $\mathbf{D} \in \mathbb{R}^{n \times N}$ ($n < N$), i.e., $\mathbf{x} = \mathbf{D}\boldsymbol{\alpha}$, where $\boldsymbol{\alpha} \in \mathbb{R}^N$ is the sparse coefficient. The inequality $n < N$ implies that the dictionary \mathbf{D} is redundant. The sparsest $\boldsymbol{\alpha}$ can be obtained through the following optimization problem:

$$\min_{\boldsymbol{\alpha}} \|\boldsymbol{\alpha}\|_0 \quad \text{subject to} \quad \|\mathbf{x} - \mathbf{D}\boldsymbol{\alpha}\|_2^2 \leq \varepsilon \quad (1)$$

where $\|\cdot\|_0$ is the ℓ_0 norm counting the number of nonzero entries in vector and $\varepsilon \geq 0$ is the error tolerance. Solving (1) is non-deterministic polynomial-time hard (NP-hard) in general. Several relaxation strategies are developed for approximating the solution of (1), such as basis pursuit [20], focal underdetermined system solver [21], and OMP [22].

The choice of dictionary plays an important role in sparse representation. One approach focuses on the mathematical model, such as undecimated wavelet [23] and discrete cosine transformation [24]. Another approach applies the learning techniques to infer the dictionary from the training set which is studied widely at present, such as the method of optimal directions [25] and K-SVD [26]. Compared with the dictionary constituted through the mathematical model, the learned dictionary from training set exhibits better performance in specific applications.

III. PROPOSED METHOD

A. PAN and MS Image Formation Models

In this paper, we assume that the PAN image \mathbf{Y}^{pan} and low-resolution MS image \mathbf{Y}_j^{ms} ($j = 1, 2, \dots, B$) have been registered, where B is the number of spectral bands in MS image. Let \mathbf{x}_j ($j = 1, 2, \dots, B$) be the patches of size $\sqrt{n} \times \sqrt{n}$ extracted from the j th band \mathbf{X}_j ($j = 1, 2, \dots, B$) of unknown high-resolution MS image \mathbf{X} and ordered as column vectors. Then, $\mathbf{x} = (\mathbf{x}_1^T, \dots, \mathbf{x}_j^T, \dots, \mathbf{x}_B^T)^T \in \mathbb{R}^{Bn \times 1}$ denotes the unknown high-resolution MS patch with B bands, where T denotes the transpose of vector or matrix. The PAN image covers all the wavelengths of the MS spectral bands, so the corresponding PAN patch $\mathbf{y}^{\text{pan}} \in \mathbb{R}^{n \times 1}$ can be modeled as the linear combination of spectral bands \mathbf{x}_j ($j = 1, 2, \dots, B$), i.e.,

$$\mathbf{y}^{\text{pan}} = \sum_{j=1}^B \omega_j \mathbf{x}_j + \mathbf{n}^{\text{pan}} \quad (2)$$

where ω_j ($j = 1, 2, \dots, B$) represents the weights with satisfying $\sum_{j=1}^B \omega_j = 1$ and \mathbf{n}^{pan} is assumed as the Gaussian noise. The weights ω_j ($j = 1, 2, \dots, B$) can be calculated from the normalized spectral response curves [27]. By introducing the auxiliary variable

$$\mathbf{W} = (\omega_1 \mathbf{I}, \omega_2 \mathbf{I}, \dots, \omega_B \mathbf{I}) \in \mathbb{R}^{n \times Bn} \quad (3)$$

(2) can be equivalently transformed as

$$\mathbf{y}^{\text{pan}} = \mathbf{W}\mathbf{x} + \mathbf{n}^{\text{pan}} \quad (4)$$

where $\mathbf{I} \in \mathbb{R}^{n \times n}$ is an identity matrix.

The low-resolution MS image can be modeled as the degraded version of the unknown high-resolution MS image. The relationship between the high- and low-resolution MS image patches can be expressed as

$$\mathbf{y}_j^{\text{ms}} = \mathbf{S}\mathbf{H}_j\mathbf{x}_j + \mathbf{n}_j^{\text{ms}}, \quad j = 1, 2, \dots, B. \quad (5)$$

In this formula, $\mathbf{y}_j^{\text{ms}} \in \mathbb{R}^{(n/\gamma^2) \times 1}$ is the patch extracted from the j th band low-resolution MS image \mathbf{Y}_j^{ms} and ordered as the column vector, γ is the spatial resolution ratio between the PAN image and low-resolution MS image, \mathbf{H}_j is the blur filter for the j th band, \mathbf{S} denotes the decimation operator, and \mathbf{n}_j^{ms} is assumed as the Gaussian noise for the j th band of low-resolution MS image. Generally, satellite imaging system has different modulation transfer function (MTF) of each MS band. The MTF is bell shaped, and its magnitude value at the cutoff Nyquist frequency is far lower than 0.5, to prevent aliasing [28]. Hence, \mathbf{H}_j ($j = 1, 2, \dots, B$) is assumed as the MTF-shaped filters with different cutoff frequency for each band. Let \mathbf{y}^{ms} be $\mathbf{y}^{\text{ms}} = ((\mathbf{y}_1^{\text{ms}})^{\text{T}}, \dots, (\mathbf{y}_j^{\text{ms}})^{\text{T}}, \dots, (\mathbf{y}_B^{\text{ms}})^{\text{T}})^{\text{T}} \in \mathbb{R}^{(Bn/\gamma^2) \times 1}$. Equation (5) can be rewritten as

$$\mathbf{y}^{\text{ms}} = \mathbf{L}^{\text{all}}\mathbf{x} + \mathbf{n}^{\text{ms}} \quad (6)$$

where $\mathbf{L}^{\text{all}} = \text{diag}(\mathbf{S}\mathbf{H}_1, \dots, \mathbf{S}\mathbf{H}_j, \dots, \mathbf{S}\mathbf{H}_B)$ and $\mathbf{n}^{\text{ms}} = ((\mathbf{n}_1^{\text{ms}})^{\text{T}}, \dots, (\mathbf{n}_j^{\text{ms}})^{\text{T}}, \dots, (\mathbf{n}_B^{\text{ms}})^{\text{T}})^{\text{T}}$.

B. Fusion With Sparsity Prior Model

The task of our method is to reconstruct the unknown high-resolution MS image patch \mathbf{x}_j ($j = 1, 2, \dots, B$) from the PAN image patch \mathbf{y}^{pan} and low-resolution MS image patch \mathbf{y}_j^{ms} ($j = 1, 2, \dots, B$) based on (4) and (6). However, (4) and (6) are underdetermined, and the regularization terms need to be introduced. Due to favorable statistic characteristics of the sparsity, the sparse regularization is applied to restrict the solution space. The sparse representation indicates that the unknown high-resolution MS image patch can be expressed as a linear combination of a few atoms. That is to say, the unknown high-resolution MS image patch $\mathbf{x} \in \mathbb{R}^{Bn \times 1}$ can be represented as $\mathbf{x} = \sum_{k=1}^N \alpha_k \mathbf{d}_{hk}^{\text{ms}}$. The atoms $\{\mathbf{d}_{hk}^{\text{ms}}\}_{k=1}^N$ consist of a dictionary $\mathbf{D}_h^{\text{ms}} = (\mathbf{d}_{h1}^{\text{ms}}, \mathbf{d}_{h2}^{\text{ms}}, \dots, \mathbf{d}_{hN}^{\text{ms}}) \in \mathbb{R}^{Bn \times N}$ ($Bn < N$) for the high-resolution MS image. Set $\boldsymbol{\alpha} = (\alpha_1, \alpha_2, \dots, \alpha_N)^{\text{T}} \in \mathbb{R}^N$; then, the patch \mathbf{x} can be rewritten as $\mathbf{x} = \mathbf{D}_h^{\text{ms}}\boldsymbol{\alpha}$. Referring to (4) and (6), the PAN image patch and low-resolution MS image patch can be expressed as

$$\mathbf{y}^{\text{pan}} = \mathbf{W}\mathbf{x} + \mathbf{n}^{\text{pan}} = \mathbf{W}\mathbf{D}_h^{\text{ms}}\boldsymbol{\alpha} + \mathbf{n}^{\text{pan}} = \mathbf{D}^{\text{pan}}\boldsymbol{\alpha} + \mathbf{n}^{\text{pan}} \quad (7)$$

$$\mathbf{y}^{\text{ms}} = \mathbf{L}^{\text{all}}\mathbf{x} + \mathbf{n}^{\text{ms}} = \mathbf{L}^{\text{all}}\mathbf{D}_h^{\text{ms}}\boldsymbol{\alpha} + \mathbf{n}^{\text{ms}} = \mathbf{D}_l^{\text{ms}}\boldsymbol{\alpha} + \mathbf{n}^{\text{ms}} \quad (8)$$

where $\mathbf{D}^{\text{pan}} = \mathbf{W}\mathbf{D}_h^{\text{ms}}$ and $\mathbf{D}_l^{\text{ms}} = \mathbf{L}^{\text{all}}\mathbf{D}_h^{\text{ms}}$ are the dictionaries for the PAN image and low-resolution MS image, respectively. Equations (7) and (8) indicate that the unknown high-resolution MS, PAN, and low-resolution MS images have the same sparse coefficients with respect to dictionaries \mathbf{D}_h^{ms} , \mathbf{D}^{pan} , and \mathbf{D}_l^{ms} , respectively.

At this moment, we assume that three dictionaries \mathbf{D}_h^{ms} , \mathbf{D}^{pan} , and \mathbf{D}_l^{ms} have been prepared. Then, the model of our method can be formularized as

$$\begin{cases} \boldsymbol{\alpha}^* = \arg \min_{\boldsymbol{\alpha}} \|\boldsymbol{\alpha}\|_0 & \text{subject to } \|\mathbf{y}^{\text{pan}} - \mathbf{D}^{\text{pan}}\boldsymbol{\alpha}\|_2^2 \leq \varepsilon_1, \\ \|\mathbf{y}^{\text{ms}} - \mathbf{D}_l^{\text{ms}}\boldsymbol{\alpha}\|_2^2 \leq \varepsilon_2 \\ \mathbf{x} = \mathbf{D}_h^{\text{ms}}\boldsymbol{\alpha}^* \end{cases} \quad (9)$$

where $\varepsilon_1 \geq 0$ and $\varepsilon_2 \geq 0$ are the error tolerances for \mathbf{y}^{pan} and \mathbf{y}^{ms} , respectively. The optimization problem in (9) can be approximately transformed as

$$\boldsymbol{\alpha}^* = \arg \min_{\boldsymbol{\alpha}} \|\boldsymbol{\alpha}\|_0 \text{ subject to } \left\| \begin{pmatrix} \mathbf{y}^{\text{pan}} \\ \mathbf{y}^{\text{ms}} \end{pmatrix} - \begin{pmatrix} \mathbf{D}^{\text{pan}} \\ \mathbf{D}_l^{\text{ms}} \end{pmatrix} \boldsymbol{\alpha} \right\|_2^2 \leq \varepsilon. \quad (10)$$

At last, the fused high-resolution MS image patch can be calculated as $\mathbf{x} = \mathbf{D}_h^{\text{ms}}\boldsymbol{\alpha}^*$. Due to fast computation speed and low complexity, the OMP is applied to solve (10). The proposed method is summarized as Algorithm 1.

C. Learning the Dictionaries \mathbf{D}^{pan} and \mathbf{D}_l^{ms}

In this section, we describe a joint learning strategy for learning the dictionaries \mathbf{D}^{pan} and \mathbf{D}_l^{ms} from the training set.

Let $\Omega = \{\mathbf{Z}^{\text{pan}}, \mathbf{Z}_l^{\text{ms}}\}$ be the training set, where $\mathbf{Z}^{\text{pan}} = (z_1^{\text{pan}}, \dots, z_i^{\text{pan}}, \dots, z_{\text{Num}}^{\text{pan}})$ and $\mathbf{Z}_l^{\text{ms}} = (z_1^{\text{ms}}, \dots, z_i^{\text{ms}}, \dots, z_{\text{Num}}^{\text{ms}})$ are the sets of PAN patches and low-resolution MS patches, respectively, z_i^{pan} and z_i^{ms} ($i = 1, 2, \dots, \text{Num}$) are the i th samples of PAN image patch and low-resolution MS image patch with B bands, and Num denotes the number of samples. According to (7) and (8), it can be seen that the PAN image and MS image have the same sparse coefficients with respect to dictionaries \mathbf{D}^{pan} and \mathbf{D}_l^{ms} . Therefore, to enforce that the PAN image and MS image have the same sparse coefficients, our dictionary learning task can be modeled as the following optimization problem:

$$\begin{aligned} \arg \min_{\{\mathbf{D}^{\text{pan}}, \mathbf{D}_l^{\text{ms}}, \mathbf{A}\}} & \|\mathbf{Z}^{\text{pan}} - \mathbf{D}^{\text{pan}}\mathbf{A}\|_F^2 + \|\mathbf{Z}_l^{\text{ms}} - \mathbf{D}_l^{\text{ms}}\mathbf{A}\|_F^2 \\ & \text{subject to } \forall i \|\boldsymbol{\alpha}_i\|_0 \leq \tau \end{aligned} \quad (11)$$

where $\mathbf{A} = (\boldsymbol{\alpha}_1, \boldsymbol{\alpha}_2, \dots, \boldsymbol{\alpha}_{\text{Num}})$ is a sparse coefficient matrix and τ is a nature number controlling the sparsity level. By introducing the auxiliary variables

$$\mathbf{D}_{\text{train}} = \begin{pmatrix} \mathbf{D}^{\text{pan}} \\ \mathbf{D}_l^{\text{ms}} \end{pmatrix} \quad \mathbf{Z} = \begin{pmatrix} \mathbf{Z}^{\text{pan}} \\ \mathbf{Z}_l^{\text{ms}} \end{pmatrix} \quad (12)$$

(11) can be rewritten as

$$\arg \min_{\{\mathbf{D}_{\text{train}}, \mathbf{A}\}} \|\mathbf{Z} - \mathbf{D}_{\text{train}}\mathbf{A}\|_F^2 \text{ subject to } \forall i \|\boldsymbol{\alpha}_i\|_0 \leq \tau. \quad (13)$$

We apply the K-SVD algorithm to solve (13). In accordance with the solver used in (10), the OMP algorithm is applied in the sparse coding stage of K-SVD. In addition, the initial dictionaries used in K-SVD consist of the randomly selected samples.

Algorithm 1: Image fusion via sparse representation

Input: The PAN image \mathbf{Y}^{pan} , the low-resolution MS image \mathbf{Y}_j^{ms} ($j = 1, 2, \dots, B$), three learned dictionaries $\mathbf{D}_h^{\text{ms}} \in \mathbb{R}^{Bn \times N}$, $\mathbf{D}^{\text{pan}} \in \mathbb{R}^{n \times N}$, and $\mathbf{D}_l^{\text{ms}} \in \mathbb{R}^{(Bn/\gamma^2) \times N}$, the global error ε , the spatial resolution ratio γ between the PAN image and low-resolution MS image, the patch size \sqrt{n} for PAN image, and the patch size \sqrt{n}/γ for low-resolution MS image.

1. For each patch \mathbf{y}^{pan} of size $\sqrt{n} \times \sqrt{n}$ and corresponding patch \mathbf{y}_j^{ms} of size $(\sqrt{n}/\gamma) \times (\sqrt{n}/\gamma)$ extracted from \mathbf{Y}^{pan} and \mathbf{Y}_j^{ms} ($j = 1, 2, \dots, B$), respectively

1) Solve the following problem by OMP:

$$\boldsymbol{\alpha}^* = \arg \min_{\boldsymbol{\alpha}} \|\boldsymbol{\alpha}\|_0 \text{ subject to } \left\| \begin{pmatrix} \mathbf{y}^{\text{pan}} \\ \mathbf{y}^{\text{ms}} \end{pmatrix} - \begin{pmatrix} \mathbf{D}^{\text{pan}} \\ \mathbf{D}_l^{\text{ms}} \end{pmatrix} \boldsymbol{\alpha} \right\|_2 \leq \varepsilon$$

where $\mathbf{y}^{\text{ms}} = ((\mathbf{y}_1^{\text{ms}})^{\text{T}}, \dots, (\mathbf{y}_j^{\text{ms}})^{\text{T}}, \dots, (\mathbf{y}_B^{\text{ms}})^{\text{T}})^{\text{T}}$.

2) Calculate the fused vector through $\mathbf{x} = \mathbf{D}_h^{\text{ms}} \boldsymbol{\alpha}^*$.

3) Reshape the vector \mathbf{x} as the high-resolution MS image patch with size $\sqrt{n} \times \sqrt{n} \times B$.

2: End

3: Generate the high-resolution MS image by averaging the overlapped pixels.

Output: High-resolution MS image \mathbf{X} .

D. Learning the Dictionary \mathbf{D}_h^{ms}

In this section, we design a novel strategy to construct the dictionary for the high-resolution MS image, since there is no real high-resolution MS image for dictionary learning.

Equations (7) and (8) imply that the dictionaries \mathbf{D}_h^{ms} , \mathbf{D}^{pan} , and \mathbf{D}_l^{ms} have the relationships: $\mathbf{D}^{\text{pan}} = \mathbf{W} \mathbf{D}_h^{\text{ms}}$ and $\mathbf{D}_l^{\text{ms}} = \mathbf{L}^{\text{all}} \mathbf{D}_h^{\text{ms}}$. Based on these relationships, the dictionary \mathbf{D}_h^{ms} for the unknown high-resolution MS image can be constructed from \mathbf{D}^{pan} and \mathbf{D}_l^{ms} through the following two optimization problems:

$$\min_{\mathbf{D}_h^{\text{ms}}} \|\mathbf{D}^{\text{pan}} - \mathbf{W} \mathbf{D}_h^{\text{ms}}\|_F^2 + \lambda \|\mathbf{D}_h^{\text{ms}}\|_F^2 \quad (14)$$

$$\min_{\mathbf{D}_h^{\text{ms}}} \|\mathbf{D}_l^{\text{ms}} - \mathbf{L}^{\text{all}} \mathbf{D}_h^{\text{ms}}\|_F^2. \quad (15)$$

The solution of (14) can be calculated by $\mathbf{D}_h^{\text{ms}} = (\mathbf{W}^{\text{T}} \mathbf{W} + \lambda \mathbf{I})^{-1} \mathbf{W}^{\text{T}} \mathbf{D}^{\text{pan}}$ which is used as the initial value of (15). Furthermore, due to the spectral characteristic of MS image, the i th atom $\mathbf{d}_{hi}^{\text{ms}}$ of dictionary \mathbf{D}_h^{ms} can be partitioned as

$$\mathbf{d}_{hi}^{\text{ms}} = \left((\mathbf{d}_{hi}^{\text{ms}}(1))^{\text{T}}, \dots, (\mathbf{d}_{hi}^{\text{ms}}(j))^{\text{T}}, \dots, (\mathbf{d}_{hi}^{\text{ms}}(B))^{\text{T}} \right)^{\text{T}} \quad (16)$$

where $\mathbf{d}_{hi}^{\text{ms}}(j) \in \mathbb{R}^{n \times 1}$ is the j th part of $\mathbf{d}_{hi}^{\text{ms}}$ with respect to the j th spectral band. Similarly, the atoms of dictionary \mathbf{D}_l^{ms} have the corresponding partition, i.e.,

$$\mathbf{d}_{li}^{\text{ms}} = \left((\mathbf{d}_{li}^{\text{ms}}(1))^{\text{T}}, \dots, (\mathbf{d}_{li}^{\text{ms}}(j))^{\text{T}}, \dots, (\mathbf{d}_{li}^{\text{ms}}(B))^{\text{T}} \right)^{\text{T}}. \quad (17)$$

Instead of (15), we study its subproblems

$$\min_{\mathbf{d}_{hi}^{\text{ms}}(j)} \|\mathbf{d}_{li}^{\text{ms}}(j) - \mathbf{S} \mathbf{H}_j \mathbf{d}_{hi}^{\text{ms}}(j)\|_2^2, \quad \text{for } j = 1, 2, \dots, B; \quad i = 1, 2, \dots, N. \quad (18)$$

The gradient descent method is used to solve (18), i.e.,

$$\mathbf{d}_{hi}^{\text{ms}}(j)_{(t)} = \mathbf{d}_{hi}^{\text{ms}}(j)_{(t-1)} + \left((\mathbf{d}_{li}^{\text{ms}}(j) - \mathbf{S} \mathbf{H}_j \mathbf{d}_{hi}^{\text{ms}}(j)_{(t-1)}) \uparrow \gamma \right) * p \quad (19)$$

where $\mathbf{d}_{hi}^{\text{ms}}(j)_{(t)}$ is the t th iterative value, $\uparrow \gamma$ denotes up-sampling by factor γ , p is a back projection filter, and $*$ is convolution. In addition, the filter p is set as the Gaussian filter. Then, at the t th iteration, the \mathbf{D}_h^{ms} can be computed as

$$(\mathbf{D}_h^{\text{ms}})_{(t)} = \begin{pmatrix} \mathbf{d}_{h1}^{\text{ms}}(1)_{(t)} & \cdots & \mathbf{d}_{hi}^{\text{ms}}(1)_{(t)} & \cdots & \mathbf{d}_{hN}^{\text{ms}}(1)_{(t)} \\ \vdots & \vdots & \vdots & \vdots & \vdots \\ \mathbf{d}_{h1}^{\text{ms}}(j)_{(t)} & \cdots & \mathbf{d}_{hi}^{\text{ms}}(j)_{(t)} & \cdots & \mathbf{d}_{hN}^{\text{ms}}(j)_{(t)} \\ \vdots & \vdots & \vdots & \vdots & \vdots \\ \mathbf{d}_{h1}^{\text{ms}}(B)_{(t)} & \cdots & \mathbf{d}_{hi}^{\text{ms}}(B)_{(t)} & \cdots & \mathbf{d}_{hN}^{\text{ms}}(B)_{(t)} \end{pmatrix} \quad (20)$$

Based on Sections III-C and III-D, the dictionary learning method for \mathbf{D}_h^{ms} , \mathbf{D}^{pan} , and \mathbf{D}_l^{ms} can be summarized as Algorithm 2.

Algorithm 2: Learning the dictionaries \mathbf{D}_h^{ms} , \mathbf{D}^{pan} , and \mathbf{D}_l^{ms}

Input: The training set $\Omega = \{\mathbf{Z}^{\text{pan}}, \mathbf{Z}_l^{\text{ms}}\}$, the sparsity level τ , the spatial resolution ratio γ between the PAN image and low-resolution MS image, the iterative number Iter , and the weight matrix $\mathbf{W} = (\omega_1 \mathbf{I}, \omega_2 \mathbf{I}, \dots, \omega_B \mathbf{I})$.

1: Learning dictionaries \mathbf{D}^{pan} and \mathbf{D}_l^{ms}

The dictionaries \mathbf{D}^{pan} and \mathbf{D}_l^{ms} are learned based on (13), which is solved by the K-SVD algorithm.

2: Learning dictionary \mathbf{D}_h^{ms}

1) Compute the solution of (14) as

$$\hat{\mathbf{D}}_h^{\text{ms}} = (\mathbf{W}^{\text{T}} \mathbf{W} + \lambda \mathbf{I})^{-1} \mathbf{W}^{\text{T}} \mathbf{D}^{\text{pan}}$$

and set $(\mathbf{D}_h^{\text{ms}})_{(0)} = \hat{\mathbf{D}}_h^{\text{ms}}$.

2) **For** $t = 1 : \text{Iter}$

The i th ($i = 1, 2, \dots, N$) atom in $(\mathbf{D}_h^{\text{ms}})_{(t-1)}$ is updated through

$$\mathbf{d}_{hi}^{\text{ms}}(j)_{(t)} = \mathbf{d}_{hi}^{\text{ms}}(j)_{(t-1)} + \left((\mathbf{d}_{li}^{\text{ms}}(j) - \mathbf{S} \mathbf{H}_j \mathbf{d}_{hi}^{\text{ms}}(j)_{(t-1)}) \uparrow \gamma \right) * p, \quad j = 1, 2, \dots, B$$

and the $(\mathbf{D}_h^{\text{ms}})_{(t)}$ is computed as (20).

End

Output: Three dictionaries \mathbf{D}_h^{ms} , \mathbf{D}^{pan} , and \mathbf{D}_l^{ms} .

IV. EXPERIMENTS AND PERFORMANCE COMPARISONS**A. Experimental Data Sets**

To evaluate the effectiveness of the proposed method, we consider two data sets acquired by QuickBird and IKONOS satellites, respectively.

1) **QuickBird:** The QuickBird satellite provides PAN image at 0.7-m spatial resolution and MS image with four bands at 2.8-m spatial resolution. The images on Sundarbans acquired on November 21, 2002, including various land cover types are used, which are downloaded at <http://glcf.umd.edu/data/quickbird/sundarbans.shtml>.

TABLE I
 NYQUIST CUTOFF FREQUENCIES OF QUICKBIRD AND IKONOS FOR
 DIFFERENT SPECTRAL BANDS

	Blue	Green	Red	NIR
QuickBird	0.34	0.32	0.30	0.24
IKONOS	0.27	0.28	0.29	0.28

- 2) IKONOS: The IKONOS satellite provides PAN image at 1-m spatial resolution and MS image with four bands at 4-m spatial resolution. The IKONOS images captured over Sichuan, China, in May 2008 are used, which are downloaded at <http://glcf.umiacs.umd.edu/data/ikonos/index.shtml>.

B. Parameter Setting

To evaluate the proposed method, both simulated and real experiments are performed. In the simulated experiments, the original PAN image and MS image are degraded first. Then, the degraded PAN image and MS image are fused, and the original MS image is used as the reference image. Through the simulated experiments, the effects of parameters on the proposed method and comparisons of various methods are analyzed and discussed. In the real experiments, the original real PAN image and MS image are fused, which aims to evaluate the performances of various methods in practice.

In QuickBird and IKONOS satellites, the spatial resolution ratio between the PAN image and low-resolution MS image is four. Therefore, the degraded PAN image is generated by downsampling the original PAN image by a factor of four in the simulated experiments. The degraded MS image is obtained by filtering the original MS image with MTF-shaped filters and then downsampling by a factor of four. The approximated Gaussian filters with different Nyquist cutoff frequencies simulate the MTF of satellite. The Nyquist cutoff frequencies of QuickBird and IKONOS for different spectral bands are listed in Table I [29].

The proposed method is compared with six popular methods: the Gram–Schmidt (GS) algorithm [30], the fast IHS (FIHS) [3], the SVT [11], the ATWT-based method with the CBD injection model [10], the AWLP [9], and the CS-based method [16]. The GS method is implemented by the software Environment for Visualizing Images [30]. The decomposition level of ATWT for CBD and AWLP-based methods is set as two. As to the SVT method, the σ^2 in the Gaussian radial basis function kernel is set to 1.2, and the parameter γ of the mapped least-squares support vector machine (LS-SVM) is set to one, which gives the best fusion results for the SVT. For our method, the global error ε of the OMP is generally chosen as $\sqrt{n} \cdot C \cdot \sigma$ [18] in noise case, where n is the length of the signal, C is a constant, and σ denotes the noise level. If the source images are clean, the global ε is set to one. The weights in (2) are set as follows [15], [31]: 1) $\omega_1 = 0.1139$, $\omega_2 = 0.2315$, $\omega_3 = 0.2308$, and $\omega_4 = 0.4239$ for QuickBird and 2) $\omega_1 = 0.1071$, $\omega_2 = 0.2646$, $\omega_3 = 0.2696$, and $\omega_4 = 0.3587$ for IKONOS. To improve the adaptability of dictionaries \mathbf{D}_h^{ms} , $\mathbf{D}_h^{\text{pan}}$, and \mathbf{D}_l^{ms} , the dictionaries are learned from the source images adaptively, i.e., the training samples are chosen from the source images directly. In the stage of learning the dictionary \mathbf{D}_h^{ms} , the iteration number

Iter controls the stopping criterion, which is set to ten in the experiments.

C. Quality Assessment Indexes

In order to quantitatively assess the fusion performance, various quality indexes are used. In the simulated experiments, five quality indexes with reference are considered. The correlation coefficient (CC) [32] and the root-mean-square error (RMSE) between the fused MS image and the reference MS image are calculated for each band. The average spectral angle mapper (SAM) [33], the erreur relative globale adimensionnelle de synthèse (or relative dimensionless global error in synthesis) (ERGAS) [34], and Q4 [35] are computed with all spectral bands. In the real experiments, the “quality with no reference” (QNR) [36] is used which consists of the spectral distortion index D_λ and the spatial distortion index D_s . The best values of CC, Q4, and QNR are one. The best values of RMSE, SAM, ERGAS, D_λ , and D_s are zero.

D. Effects of Patch Size and Dictionary Size

In this section, the effects of patch size and dictionary size on fusion performance are evaluated. The experiments are implemented on the degraded PAN image and degraded MS image. The original MS image is used as the reference image. The CC, RMSE, SAM, ERGAS, and Q4 indexes are used to assess the quality of fused images.

First, we consider the effect of patch size which directly affects the information contained in each patch. For this evaluation goal, the dictionary size is first fixed as 512. Three different patch sizes for low-resolution MS image are studied, including 2×2 , 3×3 , and 4×4 . The corresponding patch sizes of PAN image are 8×8 , 12×12 , and 16×16 , respectively. Two pairs of remote sensing images shown in Fig. 1(a) and (b) (QuickBird images) and Fig. 1(c) and (d) (IKONOS images) are fused by the proposed method with different patch sizes. Then, the quality indexes are calculated, where the average CC and RMSE of four bands are presented. In addition, all the values of indexes are normalized to the range [0, 1]. The normalized results with respect to the different patch size are plotted in Fig. 2, where the horizontal axis is the patch size of low-resolution MS image and the vertical axis is the normalized results. Larger CC and Q4 indicate better fused result, and smaller RMSE, SAM, and ERGAS indicate better fused result. Based on the curves in Fig. 2, it can be seen that the performance of proposed method is improved as the patch size increases. However, our method with bigger patch size needs more computation time.

Second, the effects of dictionary size are analyzed, i.e., the number of atoms in dictionary. Four different dictionary sizes, namely, 256, 512, 1024, and 1536, are considered. The patch sizes of low-resolution MS and PAN images are fixed as 3×3 and 12×12 , respectively. The MS image and PAN image shown in Fig. 1(a) and (b) and Fig. 1(c) and (d) are fused by the proposed method with different dictionary sizes. Fig. 3 exhibits the performance of the proposed method with different dictionary sizes. From Fig. 3, it can be seen that the proposed method with larger dictionary yields better performance with higher computational cost.

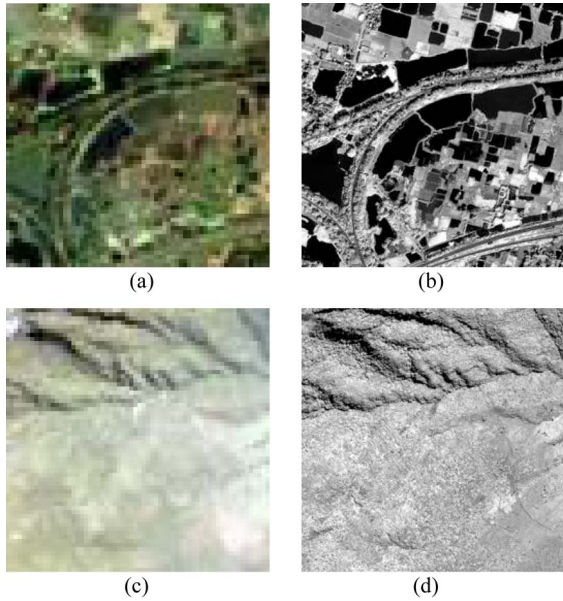


Fig. 1. Two pairs of degraded remote sensing images. (a) Degraded MS image (red, green, blue bands) of QuickBird. (b) Degraded PAN image of QuickBird. (c) Degraded MS image (red, green, blue bands) of IKONOS. (d) Degraded PAN image of IKONOS.

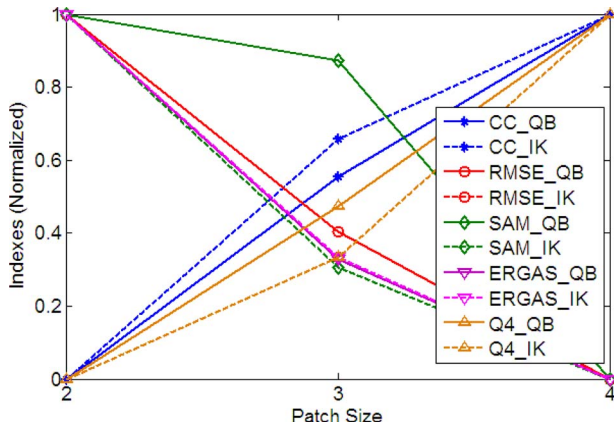


Fig. 2. Performance of the proposed method with different patch sizes. The symbols “QB” and “IK” denote the QuickBird and IKONOS, respectively.

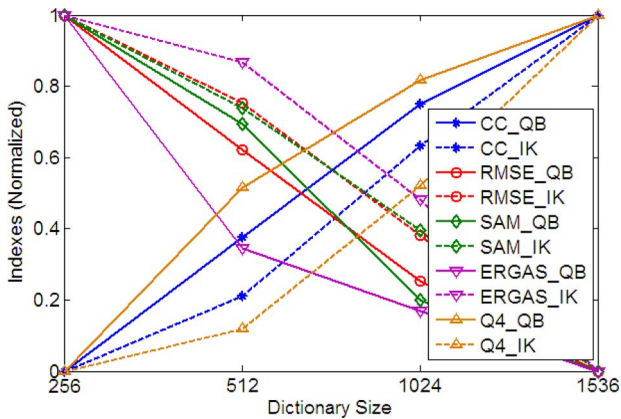


Fig. 3. Performance of the proposed method with different dictionary sizes. The symbols “QB” and “IK” denote the QuickBird and IKONOS, respectively.

Our method is implemented on the local overlapping image patch. However, all MS bands have the aliasing patterns acquired by spaceborne sensors. The insufficient overlapping re-

gion could result in that the fusion method based on sparse representation is sensitive to aliasing patterns. The aliasing patterns in source image may be transferred or even be enhanced in the final results. One direct and feasible strategy to overcome the aliasing patterns is to increase the patch size. Figs. 2 and 3 show that the performance of our method can be improved further through increasing the patch size and the dictionary size, but at higher computational cost. Therefore, the choices of patch size and dictionary size have a tradeoff between the performance and computation time. In the following experiments, the patch size of low-resolution MS image and the dictionary size are set to 3×3 and 1024, respectively.

E. Simulated Experimental Results

First, the performance of the proposed method is evaluated on a pair of simulated QuickBird images. Fig. 4(a) and (b) shows the low-resolution MS image with a resolution of 11.2 m and PAN image with a resolution of 2.8 m, respectively. The original MS image at 2.8-m resolution is used as the reference image, as shown in Fig. 4(c). The fused images of various methods are reported in Fig. 4(d)–(j). In addition, a rectangle region containing the trees and buildings is magnified and put at the left bottom of each fused image. Fig. 4(d) and (e) shows the results of the GS and FIHS methods, respectively, which exhibit spectral distortion. The results of SVT, CBD, AWLP, CS, and proposed methods are shown in Fig. 4(f)–(j), respectively. Compared with the reference image [Fig. 4(c)], the SVT, CBD, AWLP, CS, and proposed methods can preserve the spectral information effectively but lose some spatial details. Focusing on the magnified regions, our method is comparable to the SVT, CBD, AWLP, and CS methods in preserving the details. Table II lists the quality assessment of the results in Fig. 4. The best results for each quality index are labeled in bold. The results of CC and RMSE demonstrate that the proposed method produces the best match for the reference image except the near infrared band. As to the SAM index, the AWLP method provides the best result. The SVT method surpasses our method slightly in terms of the ERGAS index. Concerning the Q4 index measuring both spectral and radiometric distortions, the proposed method generates the best result.

Second, the performance of the proposed method is evaluated on a pair of simulated IKONOS images. Fig. 5(a) and (b) shows a pair of simulated images with the resolutions of 16 and 4 m, respectively. Fig. 5(c) shows the original MS image at 4-m resolution which is used as the reference image. Fig. 5(d)–(j) shows the fused images by various fusion methods. The left bottom in each fused image is a magnified rectangle region containing the mountain vegetation and canyon. Fig. 5(d) shows the result provided by the GS method which exhibits unnatural color. Fig. 5(e) loses the most detailed information provided by the FIHS method. From the magnified regions, it can be seen that the AWLP method generates the best contrast. However, some information about the canyon cannot be preserved effectively by the AWLP method. By contrast, our method provides the most characteristic of canyon, but the fused image has some aliasing patterns. Table III presents the quality indexes of the results in Fig. 5. Although the AWLP method generates the

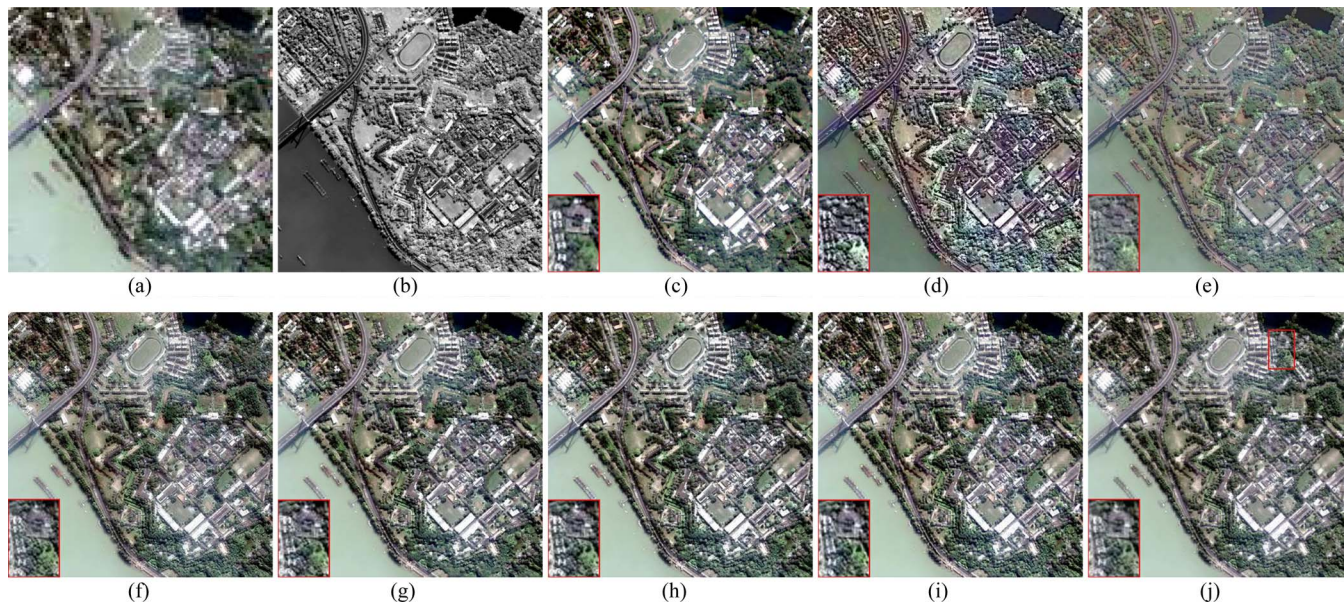


Fig. 4. Simulated QuickBird images and fused results by different methods. (a) Degraded MS image at 11.2-m spatial resolution. (b) Degraded PAN image at 2.8-m spatial resolution. (c) Original MS image at 2.8-m spatial resolution. (d) GS method. (e) FIHS method. (f) SVT method. (g) CBD method. (h) AWLP method. (i) CS method. (j) Proposed method.

TABLE II
QUANTITATIVE ASSESSMENT OF THE FUSION RESULTS IN FIG. 4

Indexes	GS	FIHS	SVT	CBD	AWLP	CS	Proposed
CC	R	0.57	0.83	0.94	0.92	0.92	0.95
	G	0.62	0.85	0.94	0.93	0.93	0.96
	B	0.56	0.84	0.94	0.93	0.92	0.96
	N	0.90	0.94	0.97	0.97	0.95	0.96
	Avg	0.66	0.87	0.95	0.94	0.93	0.96
RMSE	R	56.78	38.36	22.17	24.75	24.66	19.77
	G	55.67	37.71	21.34	23.65	24.48	19.00
	B	57.49	38.07	21.83	24.14	24.96	18.36
	N	37.20	28.81	18.05	18.33	27.86	22.62
	Avg	51.79	35.74	20.85	22.72	25.49	19.94
SAM	11.10	5.69	4.85	5.00	4.52	5.17	4.73
ERGAS	7.59	5.88	3.68	3.74	5.68	4.13	4.61
Q4	0.60	0.76	0.87	0.86	0.84	0.82	0.88

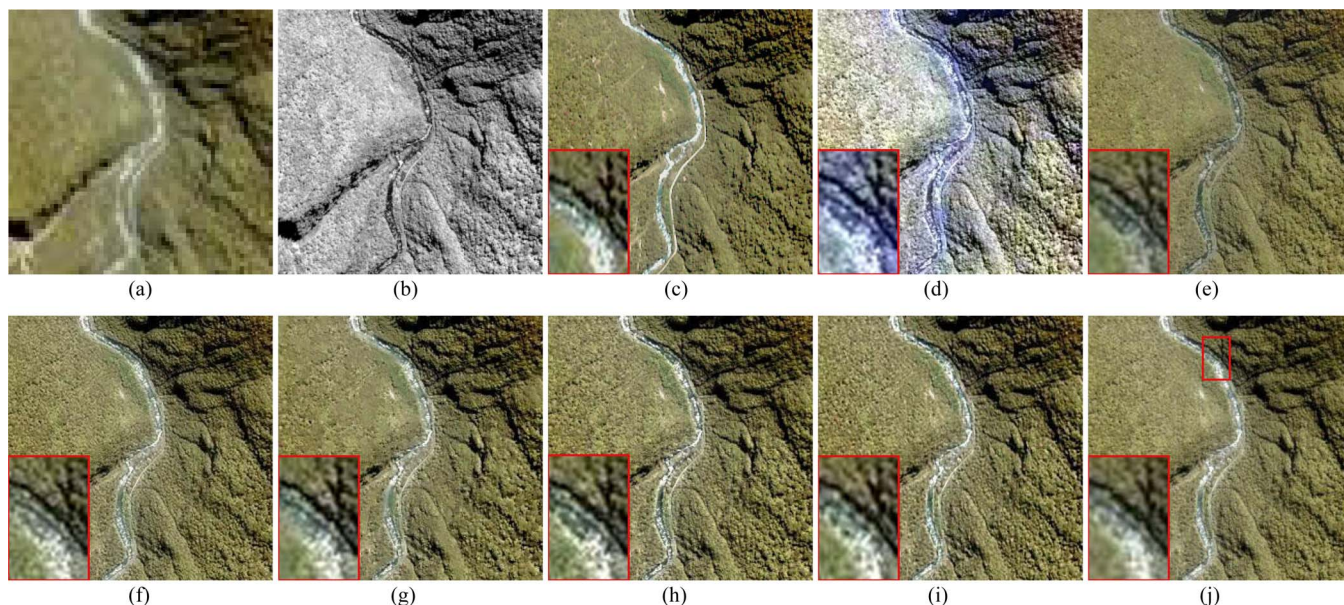


Fig. 5. Simulated IKONOS images and fused results by different methods. (a) Degraded MS image at 16-m spatial resolution. (b) Degraded PAN image at 4-m spatial resolution. (c) Original MS image at 4-m spatial resolution. (d) GS method. (e) FIHS method. (f) SVT method. (g) CBD method. (h) AWLP method. (i) CS method. (j) Proposed method.

TABLE III
QUANTITATIVE ASSESSMENT OF THE FUSION RESULTS IN FIG. 5

Indexes		GS	FIHS	SVT	CBD	AWLP	CS	Proposed
CC	R	0.83	0.87	0.90	0.90	0.88	0.88	0.92
	G	0.83	0.87	0.90	0.90	0.88	0.90	0.92
	B	0.80	0.84	0.88	0.88	0.89	0.89	0.91
	N	0.86	0.88	0.90	0.91	0.87	0.88	0.91
	Avg	0.83	0.87	0.90	0.90	0.88	0.89	0.91
RMSE	R	47.87	23.35	20.58	20.40	23.40	23.19	18.65
	G	50.75	23.34	20.51	20.52	23.07	20.17	18.45
	B	77.73	22.49	19.80	19.53	18.87	19.60	16.91
	N	35.11	26.80	24.43	24.14	32.79	27.51	23.40
	Avg	52.87	24.00	21.33	21.15	24.53	22.62	19.35
SAM		12.85	3.43	3.59	3.55	3.40	4.35	3.44
ERGAS		4.90	3.74	3.41	3.37	4.57	3.84	3.26
Q4		0.63	0.72	0.74	0.76	0.73	0.73	0.78

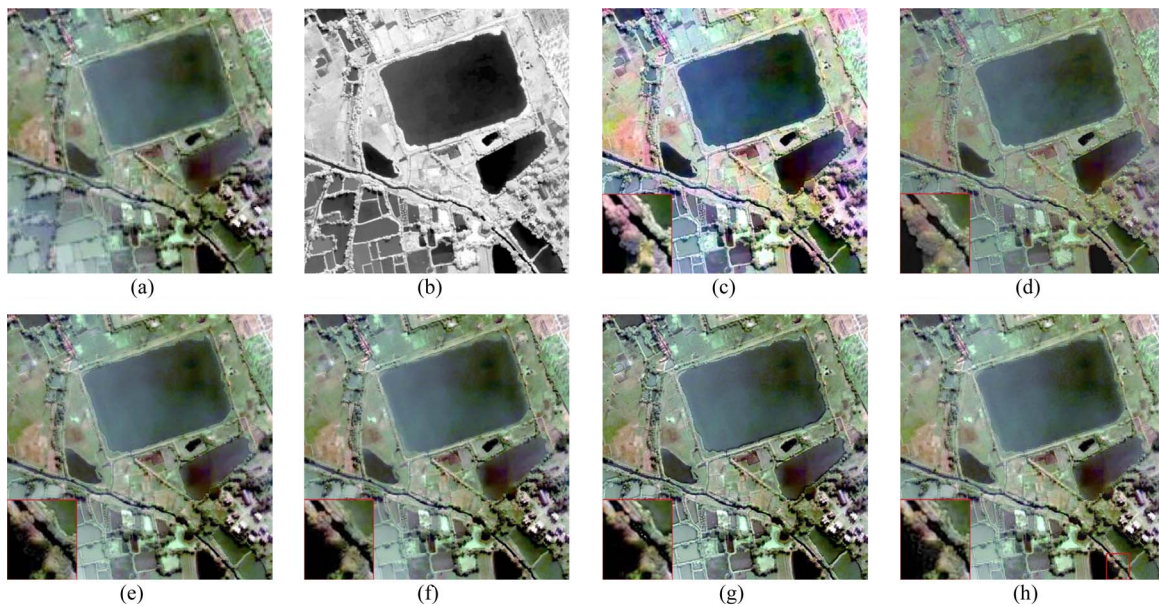


Fig. 6. Real QuickBird images and fused results by different methods. (a) MS image at 2.8-m spatial resolution. (b) PAN image at 0.7-m spatial resolution. (c) GS method. (d) FIHS method. (e) SVT method. (f) CBD method. (g) AWLP method. (h) Proposed method.

TABLE IV
QUANTITATIVE ASSESSMENT OF THE FUSION RESULTS IN FIG. 6

Indexes	GS	FIHS	SVT	CBD	AWLP	Proposed
D_λ	0.0815	0.0904	0.0808	0.0954	0.1067	0.0564
D_s	0.3124	0.2457	0.1088	0.1162	0.1539	0.0756
QNR	0.6316	0.6861	0.8192	0.7995	0.7558	0.8722

best SAM result, the best CC, RMSE, ERGAS, and Q4 results demonstrate the superiority of our method.

F. Real Experimental Results

In this section, we will evaluate the proposed method on the real remote sensing images. The quality assessment indexes without the reference image, namely, D_λ , D_s , and QNR, are used to evaluate the fused image objectively.

Fig. 6(a) and (b) shows a pair of real QuickBird images at 2.8-m (MS image) and 0.7-m (PAN image) resolutions, respec-

tively. The fused images of all tested fusion methods are shown in Fig. 6(c)–(h). Similar to the simulated experimental results, the GS and FIHS methods generate the spectral distortions, as shown in Fig. 6(c) and (d). The SVT, CBD, AWLP, and our method generate high-resolution MS images with satisfactory spectral preservation, as shown in Fig. 6(e)–(h). A magnified rectangle region containing some trees is presented at the left bottom of fused image. In this rectangle region, it is difficult to reconstruct these trees due to the large black area around the tree region in the PAN image. From the magnified rectangle regions, we can see that the trees provided by our method

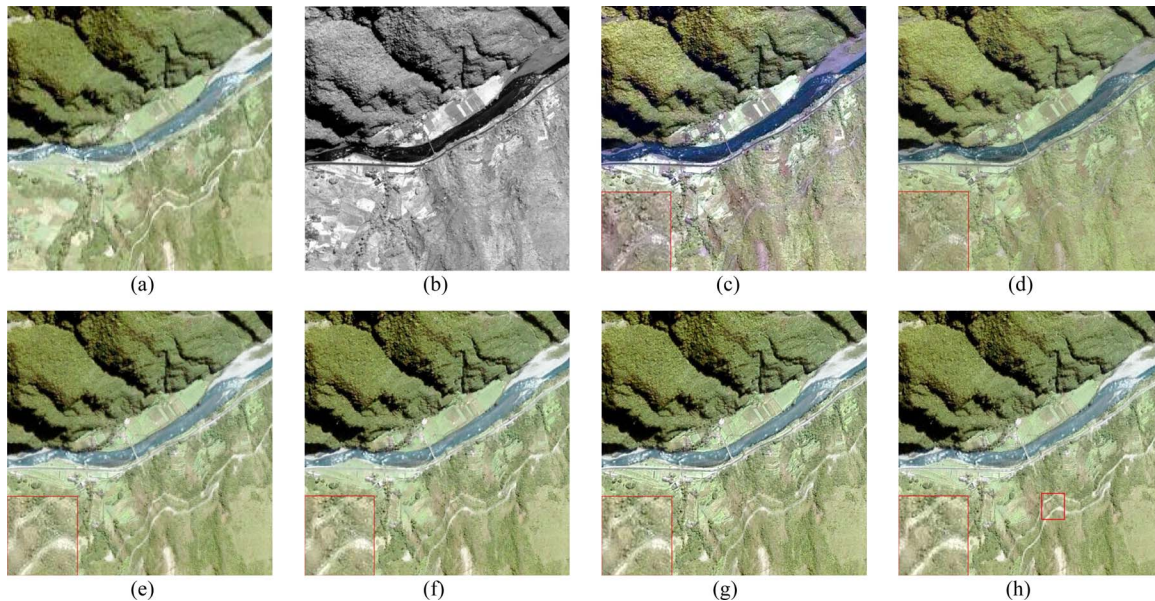


Fig. 7. Real IKONOS images and fused results by different methods. (a) MS image at 4-m spatial resolution. (b) PAN image at 1-m spatial resolution. (c) GS method. (d) FIHS method. (e) SVT method. (f) CBD method. (g) AWLP method. (h) Proposed method.

TABLE V
QUANTITATIVE ASSESSMENT OF THE FUSION RESULTS IN FIG. 7

Indexes	GS	FIHS	SVT	CBD	AWLP	Proposed
D_λ	0.2120	0.2608	0.2496	0.2047	0.2321	0.2262
D_s	0.2914	0.2918	0.1846	0.1817	0.2203	0.1498
QNR	0.5584	0.5234	0.6118	0.6507	0.5988	0.6579

are more natural. Table IV shows the QNR index results of corresponding fused images in Fig. 6. Our method generates the best D_λ , D_s , and QNR values.

Another pair of real IKONOS images is used to evaluate the performance of our method. Fig. 7(a) and (b) shows the real MS and PAN images at 4- and 1-m spatial resolutions, respectively. The corresponding results are presented in Fig. 7(c)–(h). The colors of images in Fig. 7(c) and (d) are unnatural, which are generated by the GS and FIHS methods. A rectangle region about the branch of river exhibiting haze is extracted from the fused images and magnified. From the magnified regions, it can be seen that our method is comparable to the SVT, CBD, and AWLP methods in providing the branch of river. In addition, the fused image quality is evaluated, and the corresponding results are presented in Table V. Although the CBD method provides better result in terms of the D_λ index, the best D_s and QNR values point out that our method can generate the fused image with small spectral and spatial distortions overall.

Finally, the experiments on the noisy source images are performed to study the robustness of the proposed method. One pair of clean real QuickBird images is corrupted by Gaussian noise. The standard deviation of Gaussian distribution is regarded as the noise level. Fig. 8(a) and (b) shows the noisy MS and PAN images with noise level $\sigma = 10$, respectively. Fig. 8(c)–(h) shows the corresponding results of various methods. As can be seen, our method can provide more natural

fused result [Fig. 8(h)] with fewer artifacts compared with other methods [Fig. 8(c)–(g)].

All the experiments are implemented in Matlab 7.10 and run on a Pentium 2.93-GHz PC with 2-GB memory. For fusing PAN image with size 256×256 and MS image with size $64 \times 64 \times 4$, our method may take about 15 min. The GS, FIHS, SVT, and AWLP methods need less than 1 s. The running time of the CBD method is about 30 s. Compared with the component-substitution- and multiresolution-analysis-based methods, the proposed method is time consuming. However, the algorithm can be dramatically speeded up with graphics processing unit (GPU).

V. CONCLUSION

In this paper, a restoration-based remote sensing image fusion method has been developed with the sparsity regularization. In our dictionary learning method, the dictionaries for the PAN image and low-resolution MS image are learned from the source images adaptively. The dictionary for the unknown high-resolution MS image is constructed from the dictionaries for the PAN image and low-resolution MS image. The learned dictionaries can reduce the dimensionality of dictionary, speed up the sparse decomposition, and improve the effectiveness and robustness of remote sensing image fusion. Our method can provide comparable results than other state-of-the-art methods,

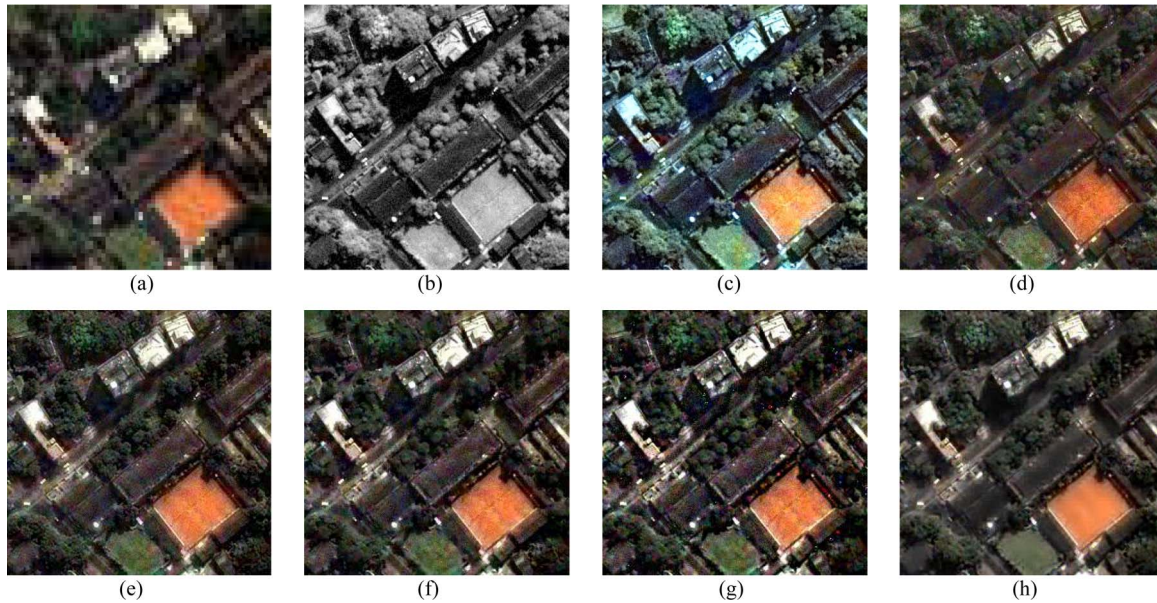


Fig. 8. Noisy source images and fused results by different methods. (a) Noisy MS image at 2.8-m spatial resolution ($\sigma = 10$). (b) Noisy PAN image at 0.7-m spatial resolution ($\sigma = 10$). (c) GS method. (d) FIHS method. (e) SVT method. (f) CBD method. (g) AWLP method. (h) Proposed method.

such as AWLP, while providing an alternative approach for remote sensing image fusion with higher computational cost. In addition, the noisy source image experiments show the robustness of the proposed method. In the future works, we focus on fast sparse recovery algorithm and multiscale dictionary learning to improve the efficiency and effect of the proposed method.

ACKNOWLEDGMENT

The authors would like to thank the editor and the anonymous reviewers for their helpful comments that led to a significant improvement in terms of both presentation and quality of this paper. The authors would also like to thank Prof. S. Zheng for providing the code of support value transform-based method and Dr. M. Vega for providing the code of the modulation transfer function.

REFERENCES

- [1] L. Wald, "Some terms of reference in data fusion," *IEEE Trans. Geosci. Remote Sens.*, vol. 37, no. 3, pp. 1190–1193, May 1999.
- [2] C. Pohl and J. L. Van Genderen, "Multisensor image fusion in remote sensing: Concepts, methods and applications," *Int. J. Remote Sens.*, vol. 19, no. 5, pp. 823–854, Mar. 1998.
- [3] T. M. Tu, P. S. Huang, C. L. Hung, and C. P. Chang, "A fast intensity–hue–saturation fusion technique with spectral adjustment for IKONOS imagery," *IEEE Geosci. Remote Sens. Lett.*, vol. 1, no. 4, pp. 309–312, Oct. 2004.
- [4] M. Choi, "A new intensity–hue–saturation fusion approach to image fusion with a tradeoff parameter," *IEEE Trans. Geosci. Remote Sens.*, vol. 44, no. 6, pp. 1672–1682, Jun. 2006.
- [5] P. S. Chavez, Jr., S. C. Sides, and J. A. Anderson, "Comparison of three different methods to merge multiresolution and multispectral data: Landsat TM and SPOT panchromatic," *Photogramm. Eng. Remote Sens.*, vol. 57, no. 3, pp. 295–303, Mar. 1991.
- [6] S. Li, J. T. Kwok, and Y. Wang, "Using the discrete wavelet frame transform to merge Landsat TM and SPOT panchromatic images," *Inf. Fusion*, vol. 3, no. 1, pp. 17–23, Mar. 2002.
- [7] P. S. Pradhan, R. L. King, N. H. Younan, and D. W. Holcomb, "Estimation of the number of decomposition levels for a wavelet-based multiresolution multisensor image fusion," *IEEE Trans. Geosci. Remote Sens.*, vol. 44, no. 12, pp. 3674–3686, Dec. 2006.
- [8] J. Núñez, X. Otazu, O. Fors, A. Prades, V. Palà, and R. Arbiol, "Multiresolution-based image fusion with additive wavelet decomposition," *IEEE Trans. Geosci. Remote Sens.*, vol. 37, no. 3, pp. 1204–1211, May 1999.
- [9] X. Otazu, M. González-Audicana, O. Fors, and J. Núñez, "Introduction of sensor spectral response into image fusion methods. Application to wavelet-based methods," *IEEE Trans. Geosci. Remote Sens.*, vol. 43, no. 10, pp. 2376–2385, Oct. 2005.
- [10] A. Garzelli and F. Nencini, "Interband structure modeling for pansharpening of very high-resolution multispectral images," *Inf. Fusion*, vol. 6, no. 3, pp. 213–224, Sep. 2005.
- [11] S. Zheng, W. Shi, J. Liu, and J. Tian, "Remote sensing image fusion using multiscale mapped LS-SVM," *IEEE Trans. Geosci. Remote Sens.*, vol. 46, no. 5, pp. 1313–1322, May 2008.
- [12] L. Alparone, L. Wald, J. Chanussot, C. Thomas, P. Gamba, and L. Bruce, "Comparison of pansharpening algorithms: Outcome of the 2006 GRS-S data-fusion contest," *IEEE Trans. Geosci. Remote Sens.*, vol. 45, no. 10, pp. 3012–3021, Oct. 2007.
- [13] J. Choi, K. Yu, and Y. Kim, "A new adaptive component-substitution-based satellite image fusion by using partial replacement," *IEEE Trans. Geosci. Remote Sens.*, vol. 49, no. 1, pp. 295–309, Jan. 2011.
- [14] M. Joshi and A. Jalobeanu, "MAP estimation for multiresolution fusion in remotely sensed images using an IGMRF prior model," *IEEE Trans. Geosci. Remote Sens.*, vol. 48, no. 3, pp. 1245–1255, Mar. 2010.
- [15] Z. Li and H. Leung, "Fusion of multispectral and panchromatic images using a restoration-based method," *IEEE Trans. Geosci. Remote Sens.*, vol. 47, no. 5, pp. 1482–1491, May 2009.
- [16] S. Li and B. Yang, "A new pan-sharpening method using a compressed sensing technique," *IEEE Trans. Geosci. Remote Sens.*, vol. 49, no. 2, pp. 738–746, Feb. 2011.
- [17] B. A. Olshausen and D. J. Field, "Emergence of simple-cell receptive field properties by learning a sparse code for natural images," *Nature*, vol. 381, no. 6583, pp. 607–609, Jun. 1996.
- [18] M. Elad and M. Aharon, "Image denoising via sparse and redundant representations over learned dictionaries," *IEEE Trans. Image Process.*, vol. 15, no. 12, pp. 3736–3745, Dec. 2006.
- [19] J. Yang, J. Wright, T. S. Huang, E. , and Y. Ma, "Image super-resolution via sparse representation," *IEEE Trans. Image Process.*, vol. 19, no. 11, pp. 2861–2873, Nov. 2010.
- [20] S. S. Chen, D. L. Donoho, and M. A. Saunders, "Atomic decomposition by basis pursuit," *SIAM Rev.*, vol. 43, no. 1, pp. 129–159, Feb. 2001.
- [21] I. F. Gorodnitsky and B. D. Rao, "Sparse signal reconstruction from limited data using FOCUSS: A re-weighted minimum norm

- algorithm,” *IEEE Trans. Signal Process.*, vol. 45, no. 3, pp. 600–616, Mar. 1997.
- [22] S. G. Mallat and Z. Zhang, “Matching pursuits with time-frequency dictionaries,” *IEEE Trans. Signal Process.*, vol. 41, no. 12, pp. 3397–3415, Dec. 1993.
- [23] J. L. Starck, J. Fadili, and F. Murtagh, “The undecimated wavelet decomposition and its reconstruction,” *IEEE Trans. Image Process.*, vol. 16, no. 2, pp. 297–309, Feb. 2007.
- [24] J. L. Starck, M. Elad, and D. L. Donoho, “Image decomposition via the combination of sparse representations and a variational approach,” *IEEE Trans. Image Process.*, vol. 14, no. 10, pp. 1570–1582, Oct. 2005.
- [25] K. Engan, S. Aase, and J. Hakon-Husoy, “Method of optimal directions for frame design,” in *Proc. IEEE Int. Conf. Acoust., Speech, Signal Process.*, 1999, vol. 5, pp. 2443–2446.
- [26] M. Aharon, M. Elad, and A. Bruckstein, “K-SVD: An algorithm for designing overcomplete dictionaries for sparse representation,” *IEEE Trans. Signal Process.*, vol. 54, no. 11, pp. 4311–4322, Nov. 2006.
- [27] R. Molina, M. Vega, J. Mateos, and A. K. Katsaggelos, “Variational posterior distribution approximation in Bayesian super resolution reconstruction of multispectral images,” *Appl. Comput. Harmon. Anal.*, vol. 24, no. 2, pp. 251–267, Feb. 2008.
- [28] B. Aiazzi, L. Alparone, S. Baronti, A. Garzelli, and M. Selva, “MTF-tailored multiscale fusion of high-resolution MS and Pan imagery,” *Photogramm. Eng. Remote Sens.*, vol. 72, no. 5, pp. 591–596, May 2006.
- [29] M. M. Khan, L. Alparone, and J. Chanussot, “Pansharpening quality assessment using the modulation transfer functions of instruments,” *IEEE Trans. Geosci. Remote Sens.*, vol. 47, no. 11, pp. 3880–3891, Nov. 2009.
- [30] C. A. Laben and B. V. Brower, “Process for enhancing the spatial resolution of multispectral imagery using pan-sharpening,” U.S. Patent 6011 875, Jan. 4, 2000.
- [31] M. Vega, J. Mateos, R. Molina, and A. K. Katsaggelos, “Super resolution of multispectral images using ℓ_1 image models and interband correlations,” *J. Signal Process. Syst.*, vol. 65, no. 3, pp. 509–523, Dec. 2011.
- [32] T. Ranchin, B. Aiazzi, L. Alparone, S. Baronti, and L. Wald, “Image fusion—the ARSIS concept and some successful implementation schemes,” *ISPRS J. Photogramm. Remote Sens.*, vol. 58, no. 1/2, pp. 4–18, Jun. 2003.
- [33] R. H. Yuhas, A. F. H. Goetz, and J. W. Boardman, “Discrimination among semi-arid landscape endmembers using the spectral angle mapper (SAM) algorithm,” in *Proc. Summar. 4th JPL Airborne Earth Sci. Workshop*, 1992, pp. 147–149.
- [34] L. Wald, T. Ranchin, and M. Mangolini, “Fusion of satellite images of different spatial resolutions: Assessing the quality of resulting images,” *Photogramm. Eng. Remote Sens.*, vol. 63, no. 6, pp. 691–699, 1997.
- [35] L. Alparone, S. Baronti, A. Garzelli, and F. Nencini, “A global quality measurement of pan-sharpened multispectral imagery,” *IEEE Geosci. Remote Sens. Lett.*, vol. 1, no. 4, pp. 313–317, Oct. 2004.
- [36] L. Alparone, B. Aiazzi, S. Baronti, A. Garzelli, F. Nencini, and M. Selva, “Multispectral and panchromatic data fusion assessment without reference,” *Photogramm. Eng. Remote Sens.*, vol. 74, no. 2, pp. 193–200, Feb. 2008.



Shutao Li (M'07) received the B.S., M.S., and Ph.D. degrees in electrical engineering from Hunan University, Changsha, China, in 1995, 1997, and 2001, respectively.

From May to October 2001, he was a Research Associate with the Department of Computer Science, The Hong Kong University of Science and Technology, Kowloon, Hong Kong. From November 2002 to November 2003, he was a Postdoctoral Fellow with the Royal Holloway College, University of London, London, U.K. Since 2001, he has been with the College of Electrical and Information Engineering, Hunan University, where he is currently a Full Professor. He has authored or coauthored more than 130 refereed papers. His research interests include information fusion, image processing, and pattern recognition.



Haitao Yin received the B.S. and M.S. degrees in applied mathematics from Hunan University, Changsha, China, in 2007 and 2009, respectively, where he is currently working toward the Ph.D. degree in the College of Electrical and Information Engineering.

His research interests include image processing and sparse representation.



Leyuan Fang (S'10) received the B.S. degree in electrical engineering from Hunan University of Science and Technology, Xiangtan, China, in 2008. Since 2008, he has been working toward the Ph.D. degree in the College of Electrical and Information Engineering, Hunan University, Changsha, China.

Since September 2011, he has been a Visiting Ph.D. Student with the Department of Ophthalmology, Duke University, Durham, NC, supported by the China Scholarship Council. His research interests include sparse representation and multiresolution analysis applied to biomedical images and remote sensing images.